Research Article | Vol. 26, No. 23 | 12 Nov 2018 | OPTICS EXPRESS 29638
Optics EXPRESS

Plasmo-thermomechanical radiation detector with on-chip optical readout

QIANCHENG ZHAO,[1] MOHAMMAD WAHIDUZZAMAN KHAN,[1] SHIVA FARZINAZAR,[2] JAEHO LEE,[2] AND OZDAL BOYRAZ[1,*]

[1]*Department of Electrical Engineering and Computer Science, University of California, Irvine, California 92697, USA*
[2]*Department of Mechanical and Aerospace Engineering, University of California, Irvine, California 92697, USA*
[*]*oboyraz@uci.edu*

Abstract: Plasmonic structures have long proved their capabilities to concentrate and manipulate light in micro- and nano-scales that facilitate strong light-matter interactions. Besides electromagnetic properties, ultra-small plasmonic structures may lead to novel applications based on their mechanical properties. Here we report efficient coupling between optical absorption and mechanical deformation in nanoscales through plasmonically enhanced fishbone nanowires. Using tailorable absorbers, free-space radiation energy is converted into heat to thermally actuate the suspended nanowires whose deformation is sensed by the evanescent fields from a waveguide. The demonstration at 660 nm wavelength with above 30% absorption shows the potential of the device to detect nW/√Hz power in an uncooled environment.

1. Introduction

The fundamental mechanism of infrared detection is energy transduction from the electromagnetic domain to others. Depending on the energy transduction mechanism, most of the infrared detectors can be classified as either photon detection or thermal sensing [1]. The semiconductor-based photonic detectors [2–4] have the advantages of high signal-to-noise ratio and fast response time. However, these advantages come at the expense of bulkiness, high cost, and power-inefficiency due to the use of cryogenic cooling. On the other hand, thermal detectors that utilize the temperature-induced changes in material properties are less expensive, more power efficient, and compatible with room temperature operations. Up to date, several uncooled thermal detectors have been demonstrated based on pyroelectricity [5–7], thermoelectricity [8–10], conductivity [11–14], piezoelectricity [15], optical resonance [16], mechanical deflection [17,18], etc. Thermo-mechanical detectors rely on the structural deformation upon exposure to radiation. As structure sizes go into nanoscales, finding an efficient light concentrator that can generate enough temperature gradient in subwavelength dimensions becomes one of the fundamental challenges. Fortunately, the plasmonic structures address this challenge by enhancing the light-matter interaction and boosting the absorption [19,20] in nanoscales. Another challenge lies in converting the tiny mechanical deflection into a measurable quantity. In doing so, optical approaches often utilize trigonometry [21,22] and interferometry [23,24] to amplify the displacement. However, these optical systems require discrete bulky lenses and detectors, hence they are difficult to miniaturize. Therefore, it is highly desirable to have efficient actuation in plasmonic nanomechanical structures with compact and sensitive on-chip transduction [25–27] and on-chip optical readout.

#338020 https://doi.org/10.1364/OE.26.029638
Journal © 2018 Received 9 Jul 2018; revised 28 Sep 2018; accepted 30 Sep 2018; published 29 Oct 2018

Optics EXPRESS

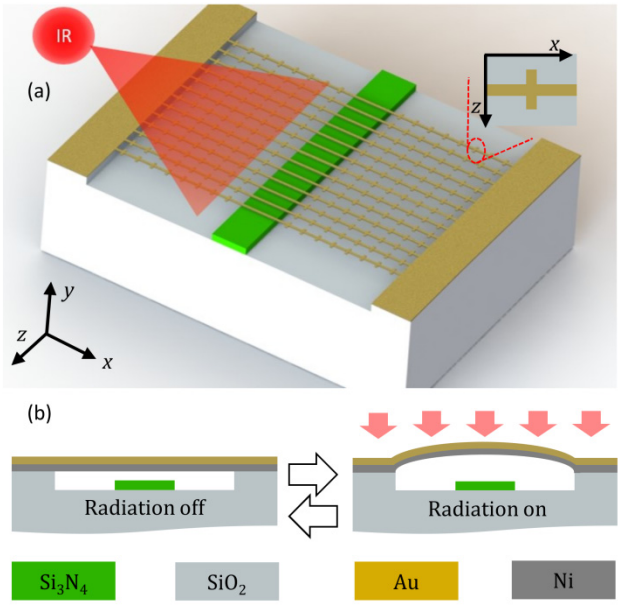

Fig. 1. (a) Schematic view: an array of bimetallic fishbone nanowires is suspended above a Si_3N_4 waveguide. The incident radiation is selectively absorbed by the plasmonic structure whose unit cell is shown in the inset. (b) The absorbed energy is converted into heat and thermally actuates the nanowires, changing the gap between the nanowire and the waveguide top surface.

This work presents an approach to combine plasmonic thermo-mechanical oscillations with on-chip optical readout in a silicon nitride (Si_3N_4) platform. In particular, we demonstrate that plasmo-thermomechanical vibrations can be monitored by using the perturbations induced on the guided modes of a Si_3N_4 waveguide, as depicted in Fig. 1(a). The operation of the detector needs the interplay of three key elements: strip antennas, bimetallic fishbone nanowires, and a waveguide. An array of nanostrip antennas (inset in Fig. 1(a)) are designed as efficient radiation absorbers that convert optical power into heat. The local heating then generates thermal gradient along the nanowires that connect the nanostrip antennas. Thermomechanical coupling is realized by the bimetallic nanowires (gold and nickel) that have different thermal expansion coefficients. Due to the mismatch of the thermal expansion coefficients of two metallic layers, the nanowire bends in response to a thermal gradient along the nanowire, as depicted in Fig. 1(b). The mechanical displacement of the suspended nanowires is sensed by an underneath waveguide if its evanescent fields interact with these nanowires. In the proposed design, the double-clamped nanowires are suspended slightly above the waveguide so that they can interact with the waveguide evanescent fields but do not stick on the waveguide, leaving a tiny gap (60 nm) between the nanowire bottom surface and waveguide top surface. The periodic arrangement of the nanowires induces optical emission of the guided modes just like grating antennas [28], and hence induces loss on the guided mode. As the thermal deflection happens, the gap between the nanowires and the waveguide varies, changing the interaction strength with the evanescent fields and thus modulating the waveguide attenuation. By monitoring the waveguide output power, the existence of radiation that generate thermo-mechanical vibrations can be detected. The waveguide power readout can be realized by on-chip silicon or germanium photodetectors [29] that are compatible with Si_3N_4 photonic platforms. Therefore, the free-space radiation can be detected in chip scale by integrating on-chip photodetectors with our device.

Optics EXPRESS

2. Device model

The proposed plasmo-thermomechanical device is composed of a Si_3N_4 waveguide which has a cross-section of 1.5 μm × 0.3 μm and has an array of suspended bimetallic fishbone nanowires that are made of gold (Au) top layer and nickel (Ni) bottom layer. The reason to use Au and Ni is because they are chemical resistant to hydrogen fluoride (HF) acid etching which is a critical step to realize nanowire suspension. Since Au has a larger thermal expansion coefficient (14.2×10^{-6}/K) than Ni (13.4×10^{-6}/K), Au is placed on top of Ni so that the nanowire bends upward to avoid collapsing or sticking to the waveguide surface. The amount of the deflection of nanowires is determined by the thickness of each layer, the temperature gradient profile, and the length of the nanowire. Both the simulation and the analytical solutions show that the ratio of the Au and Ni layer thickness should be 3/2 to yield the highest displacement [30]. The thermomechanical design concludes that the nanowire should have 30 nm thick Au, 20 nm thick Ni, with additional 3 nm Ti for adhesion purposes for optimal design. The choice of the materials also lays the ground for plasmonic design, where the gold layer at the top can interact with incoming radiation and facilitate surface plasmons.

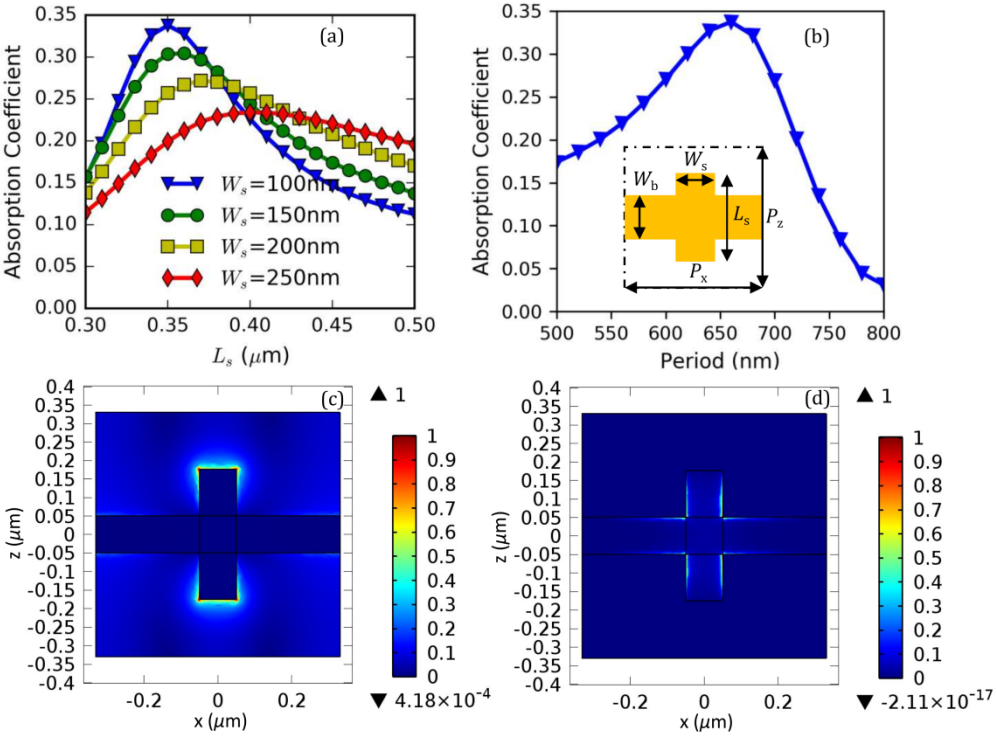

Fig. 2. (a) The absorption coefficient as a function of the strip length L_s and strip width W_s for a given period of $P_x = P_z = 660$ nm. The width of the nanobeam W_b is fixed to be 100 nm. (b) The absorption coefficient as a function of the period for a given strip length $L_s = 350$ nm and strip width $W_s = 100$ nm. The inset in (b) shows the antenna unit cell in top view. (c) The normalized electric near fields at the top surface of the antenna in the unit cell with the optimized parameters adopted from (a) and (b). The fields are enhanced at the tips of the nanostrip antenna. (d) The normalized ohmic loss distribution at the antenna top surface in the unit cell. Most of the power is dissipated along the edges of the cross.

To thermally actuate the suspended nanowires, strip antennas are employed to absorb the radiation energy. In order to increase the total absorbed energy, multiple strip antennas are periodically connected by a single nanobeam, yielding a fishbone-like nanowire. The

Optics EXPRESS

absorption of the strip antenna is optimized in a unit cell with respect to the strip length L_s, strip width W_s, and periods in both x and z directions, P_x and P_z (inset in Fig. 2(b)) at the wavelength of 785 nm. Here, the absorption coefficient is calculated as the ratio of the total ohmic loss to the incident power in the unit cell. The bimetallic cross is assumed to be suspended 360 nm above the SiO_2 substrate. The width of the nanobeam Wb is fixed to be 100 nm after optimization. As shown in Fig. 2(a), a wider strip antenna has a longer resonance length and a lower peak absorption coefficient due to its larger reflection area. Thus, a narrower strip antenna is preferred in terms of absorption coefficient. Besides the strip length and width, the absorption coefficient is also determined by the periodicity that affects the inter-antenna coupling. The absorption coefficient reaches a peak value of $C_{absp} = 0.338$ when both P_x and P_z equal 660 nm as depicted in Fig. 2(b). Figure 2(c) shows the electric near field distribution at the top surface of the antenna in the unit cell with the optimized parameters of $L_s = 350$ nm, $W_s = 100$ nm, $P_x = P_y = 660$ nm. The electric fields are enhanced at the tips of the nanostrip antenna, as expected. Figure 2(d) presents the ohmic loss distribution at the antenna top surface in the same unit cell. Most of the power is dissipated along the edges of the cross, which aligns with the current distributions. Since the fishbone antenna is suspended above the substrate, we also evaluate if the reflection from the substrate affects the near field distribution, and correspondingly, the magnitude of the absorption coefficient or not. The results show that the absorption coefficient remains relatively stable when the gap between the antennas and the SiO_2 substrate varies from 250 nm to 450 nm, as shown in Fig. 3(a). This is because the antenna metal surface acts as a mirror, and the interference between the incident and the partial reflected waves happens in the region above the antenna surface. Beneath the antenna, the incident wave no longer resembles a plane wave due to the disturbance of the antenna. Therefore, the interference caused by the reflected wave from the substrate does not influence the antenna absorption coefficient severely. To prove that, the electric near field distribution in the y-z plane is plotted in Fig. 3(b). This result is of interest as it predicts that robustness of the device absorption coefficient against the fabrication errors that affect the gap size. To emphasize the importance of the strip antenna, we compared the absorption spectrum of the unit cell with and without the strip antenna in Fig. 3(c), highlighting how the plasmonic structures can enhance the absorption at resonance despite the subwavelength thickness of the antennas. It is worth noting that the device designed here is for 785 nm, but it can be scaled to other wavelengths as well by choosing appropriate parameters. Based on the optimized unit cell size, 19 strip antennas are arranged in a row, yielding a 12.54 μm long fishbone wire. However, 3 unit cells in the wire center do not have strip antennas. The space is left for the waveguide underneath to avoid excess waveguide loss. The waveguide mode profile in the x-y plane is presented in Fig. 3(d). The evanescent field interaction with the nanowire, which is the fundamental mechanism to modulate the waveguide attenuation, can be observed from the picture.

With the help of the strip antennas, the radiation energy is efficiently absorbed and converted into thermal gradient along the nanowires that creates mechanical perturbations on the gap between the wire and the waveguide. Without perturbation, the gap is 60 nm. Not only the displacement of the nanowire affects the interaction with the evanescent field from the waveguide, but also is the number of the nanowires. Too few wires limit the modulation strength while too many wires cause extensive attenuation of the waveguide output power such that weak modulations will be buried under noise [30]. In both cases, the waveguide output power swing will be reduced. As a compromise between the evanescent field modulation strength and the waveguide propagation loss, 13 fishbone nanowires are grouped in an array in pursuit of maximizing the power swing at the waveguide output.

Optics EXPRESS

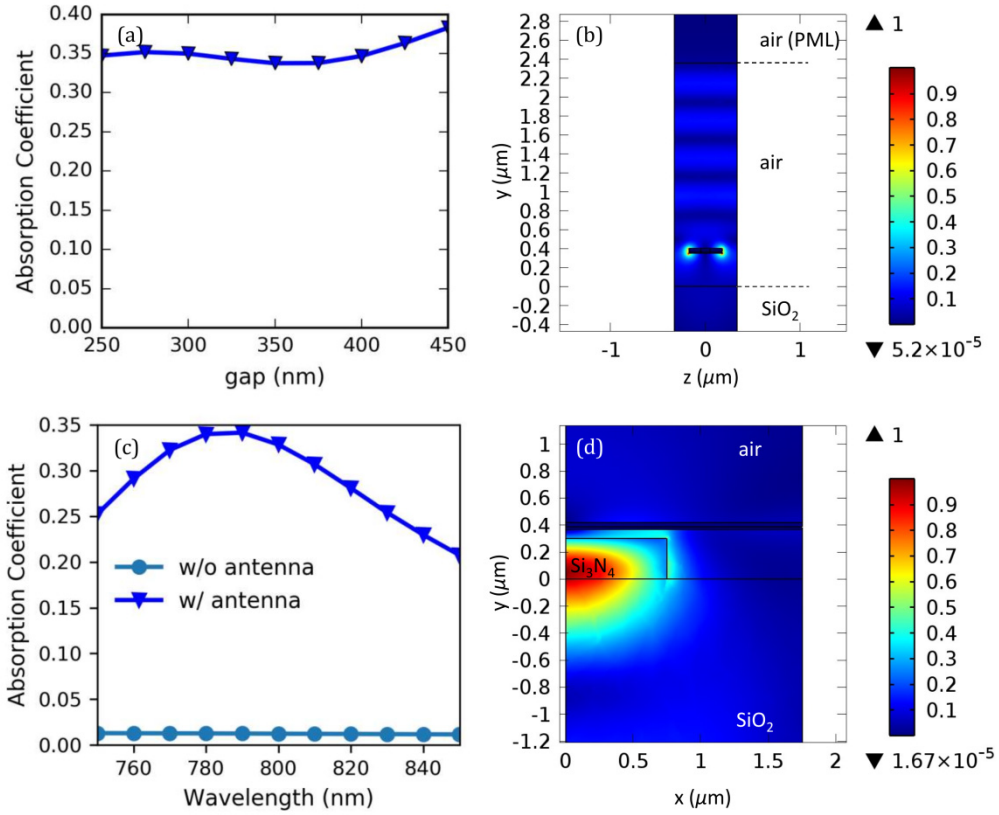

Fig. 3. (a) The absorption coefficient as a function of the gap between the nanowire and the substrate. The antenna unit cell has L_s = 350 nm, W_s = 100 nm, and P_x = P_y = 660 nm. (b) Electric field distribution in the *y*-*z* plane in the unit cell. Interference patterns can be observed in the region between the surface current source (at the boundary between air and air PML blocks, PML: perfect matched layer) and the antenna top surface. The field distribution beneath the antenna no longer resembles a plane wave due to the disturbance of the antenna. (c) The absorption coefficient with and without the strip antenna are compared. The absorption coefficient is boosted over 30 times. (d) The waveguide mode electric field distribution in the *x*-*y* plane. Only half of the structure is simulated to relax computing constrains. Evanescent field interaction with the suspended nanowire (black lines above the waveguide) can be observed clearly.

3. Device fabrication

The fabrication starts with the thermal oxidation of commercial 4-inch Si wafers. After growing 4 μm thick SiO_2 substrate, A 300 nm Si_3N_4 layer is deposited on top of the substrate using low pressure chemical vapor deposition (LPCVD) method. The Si_3N_4 waveguides are patterned with SPR 700 positive photoresist by the Karl Suss MA6 lithography machine, and then etched by the fluorine reactive ion etching (RIE). To create the desired suspended wires, SiO_2 is used as the sacrificial material due to its ease of deposition and etching. Plasma-enhanced chemical vapor deposition (PECVD) method is used to deposit a layer of 600 nm SiO_2 on the wafer with waveguide patterns. The SiO_2 top surface bumps, caused by the waveguides, must be removed to make a flat platform for the fabrication of the suspension layer. Chemical mechanical polishing (CMP) is used to flatten the wafer surface and thin the sacrificial layer. Further thinning is done by dry etching to reduce the distance between the waveguide top surface and the nanowire bottom surface. The final distance is measured to be 61.96 nm. The nanowires are patterned by using E-beam lithography, deposited by Ti, Ni, and Au layers, and then lifted off by 1-methyl-2-pyrrolidone solvent (NMP). Hydrogen fluoride

Optics EXPRESS

(HF) vapor etching is performed to etch away the SiO_2 underneath the nanowires in order to create suspended nanowires. The SEM images of the fabricated device are shown in the Fig. 4(a) and 4(b).

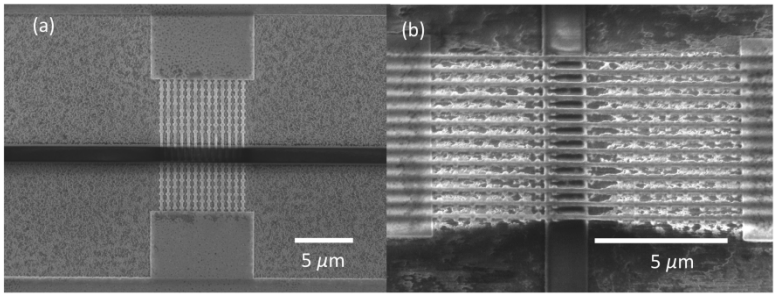

Fig. 4. (a) Top view of the scanning electron microscopy (SEM) images of the fabricated detector and its supporting anchors. There is about 800 nm misalignment between the nanowire center and the waveguide center. (b) The 30° tilted view of the SEM image of the fabricated device. The wires are straight without any breaking, indicating successful suspension. The roughness of the SiO_2 substrate is caused by the hydrofluoric acid vapor etching. The etching process does not deteriorate the surface roughness of the Si_3N_4 waveguide, therefore has negligible impact on the waveguide propagation loss.

4. Experimental characterization

Since the devices have suspended structures, it is critical to avoid dust stuffing into the gaps between the nanowires and the waveguide during experimental characterizations. Thus, a laminar air flow chamber (the dashed block in Fig. 5) is used to protect the device and the experimental setup from dust. A continuous wave (CW) laser operating at 1550 nm wavelength is fed into the waveguide via a tapered lensed fiber (TLF), serving as the probe light to generate evanescent fields and to carry the modulated information. A fiber polarization controller (FPC) is inserted between the laser source and the TLF for polarization manipulation to maximize the coupling. The output light from the waveguide is collected by another TLF, and the collected power is measured by an optical power meter. Due to fabrication errors such as antenna dimensions and variations in permittivity of deposited materials, we observe blue shift in the absorption peak. The measurements presented here are performed at 660nm by using the readily available laser diode that is hold by a laser diode mount (LDM). The laser diode is controlled by a temperature controller (TEC) and a laser diode controller (LDC). A function generator provides modulation signals to the LDC to vary the current. The generated laser beam is collected and collimated by an objective lens, and then redirected to the device with the help of three mirrors. The radiation beam is normally incident to the device surface, and its polarization (black arrows in Fig. 5) aligns with the antenna directions. The experiment setup is illustrated in Fig. 5 [31].

Optics EXPRESS

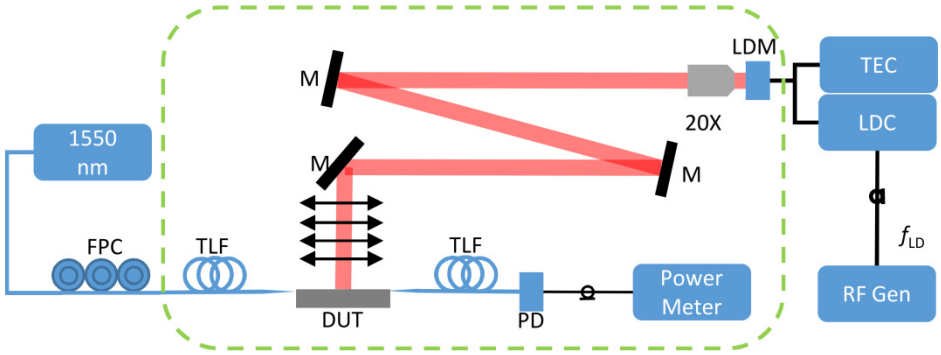

Fig. 5. Schmatic of the experiment setup. 1550 nm: CW laser at 1550 nm wavelength; FPC: fiber polarization controller; TLF: tapered lensed fiber; DUT: device under test; PD: photodiode; M: mirror; 20X: objective lens with 20X magnification; LDM: laser diode mount; TEC: temperature controller; LDC: laser diode controller; RF Gen: function generator. The dashed circle encloses the setups that are protected by the air chamber.

To assess the performance, we measure the detector bandwidth, responsivity and analyze its noise performance. In order to measure the bandwidth of the detector, a function generator was employed to drive the laser diode at different frequencies. We also used a lock-in amplifier at the detection side to record the voltage output from the optical power meter that is synchronized to the function generator. The normalized voltages are plotted against frequencies as shown in Fig. 6(a). We calculate the 3dB bandwidth of the detection scheme as 9.6 Hz. The bandwidth corresponds to a time constant $\tau = 1/(2\pi f_{3dB}) = 16.6$ ms, which correlates well with other thermal IR detectors [23,32] whose time constants are also in the order of milliseconds.

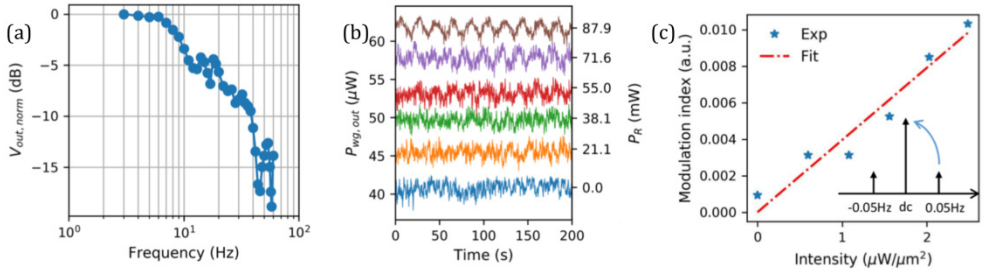

Fig. 6. (a) The normalized output voltage as a function of the modulation frequency. The voltage readout is displayed on a lock-in amplifier that is connected to the analog output of the power meter which measures the waveguide output power. (b) The waveforms of the waveguide output power $P_{wg,out}$ as a function of time and the radiation power P_R. Time traces of $P_{wg,out}$ at different biases have similar average power but are offset along the y axis for clarity. The ticks in the right y axis label the radiation power. Tick 0 represents non-illumination case. (c) The modulation index as a function of the peak intensity. The inset shows the definition of the modulation index. Only positive frequency is used in calculation.

Another important characteristic for the detector is its responsivity, which characterizes how efficiently the detector can respond to a radiation change and convert it to a waveguide output power variation. We use a sinusoidally modulated radiation light at 0.05 Hz. Using the modulated light instead of the static light can help avoid power drift problem that is often caused by the instability of the mechanical stages. On the other hand, the slowly modulated signal resembles the dc condition, which is representative for the characterization of the device low frequency performance. Figure 6(b) shows the waveform of the waveguide output power, $P_{wg,\,out}$, as a function of time and radiation light power, P_R. The traces are biased at different positions for clarity. The ticks on the right y-axis label the radiation powers. As the

Optics EXPRESS

radiation power becomes larger, the waveform of P_{wg} shows a clearer signature of the modulation. The case when $P_R = 0$ corresponds to the non-illumination condition. Under such condition, the detector is in a free-running status, and the fluctuation on the $P_{wg,out}$ should be caused by noise only. To quantify the responsivity of the detector, the ratio of the modulation index on the waveguide output power to the radiation intensity is being used. Here, the modulation index is defined by normalizing the coefficient at + 0.05 Hz to its dc coefficient (inset in Fig. 6(c)). Considering that the beam intensity follows Gaussian profile and that the device area is smaller than the beam area, the light intensity that the device receives is assumed to be the peak intensity in the center of the beam. Guided by the definition, the sensitivity of the detector is plotted in Fig. 6(c). The fitted curve (red dashed line) has a slope of 0.003954 $\mu m^2/\mu W$, which is the responsivity of the device, indicating that 1 $\mu W/\mu m^2$ radiation intensity change will result in an increment of 0.003954 modulation index. Theoretically, the case when there is no intensity should have zero modulation index, but in fact it exhibits a non-zero value due to noise.

In our previous work for a mid-infrared detector [30], we defined the figure of merit (FOM) of a detector as the ratio of the change of the S_{21} parameter to the change of the incident infrared radiation intensity, namely, $\Delta S_{21}/\Delta I_{IR}$, to characterize the sensor responsivity. Here, the modulation index is used instead of the ΔS_{21}, simply because it is easy to calculate in digital processing and straightforward to present in the paper. The responsivity defined in this paper is ¼ of the FOM in Ref [30], because (i) only positive frequency coefficient is used for calculation, so the responsivity is reduced half by nature; (ii) the positive frequency coefficient is converted from the amplitude of the modulation in time domain, while the change of the S_{21} parameter counts on full-swing of the modulation which is twice the amplitude value. Therefore, the responsivity of this presented device is 0.003954 $\mu m^2/\mu W$, which is equivalent to 1.58×10^{-2} $\mu m^2/\mu W$ in terms of FOM. The converted FOM value is in the same order of our prediction of FOM, 2.64×10^{-2} $\mu m^2/\mu W$, for the mid-infrared detector using a similar structure. Considering the fabrication and material variations in real world, the simulation and the experimental results correlate reasonably well.

5. Noise analysis

The noise equivalent power (NEP) measures the smallest optical power that can be detected and it is defined as the input signal power that results in a signal-to-noise ratio of 1 in 1 Hz bandwidth. In our detection system, there are two main sources of noise: device noise and system noise. The fundamental sources of the device noise are the thermal fluctuation noise, background fluctuation noise, and thermomechanical noise. The thermal fluctuation noise, $\overline{P_{th}}$, caused by the random fluctuation in temperature due to the statistical nature of heat exchange between the nanowires and the environment [21], is 4.345 pW/√Hz. The background fluctuation noise, $\overline{P_{rad}}$, originating from the radiative heat exchange with the environment, is found to be 25.57 fW/√Hz. The thermo-mechanical noise, $\overline{P_{vib}}$, coming from the random vibration of the nanowires, is 312.7 pW/√Hz. The total noise power, $\overline{P_D}$, from device can be calculated by the following equation:

$$\overline{P_D} = \sqrt{\left(\frac{\overline{P_{th}}}{C_{absp}}\right)^2 + \left(\frac{\overline{P_{rad}}}{C_{absp}}\right)^2 + \left(\overline{P_{vib}}\right)^2}. \quad (1)$$

By plugging in the values calculated above and taking the antenna absorption coefficient C_{absp} into consideration, the device level noise equivalent power is calculated to be 312.9 pW/√Hz. The calculation details of the device noise from each contribution can be found in Appendix.

Optics EXPRESS

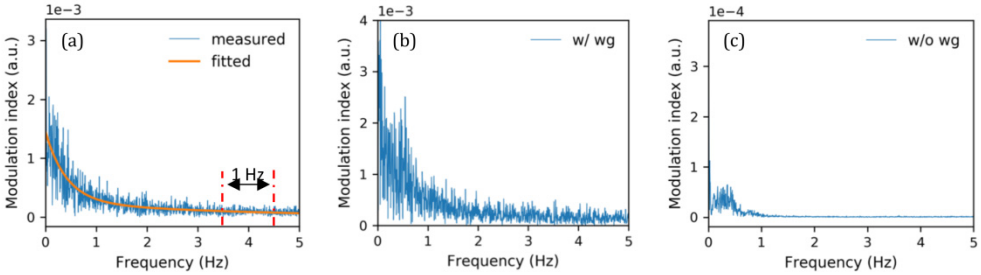

Fig. 7. (a) The normalized noise power spectrum is used to quantify NEP. The NEP is calculated based on the average noise power at 4 Hz within 1 Hz bandwidth. The noise trend line is denoted in orange. The 1/*f* noise can be clearly observed. (b) The normalized power spectrum from a bare waveguide without suspended nanowire array. Its profile and magnitude are similar to the one in (a), indicating that the device noise is negligible compared to the system noise. (c) The normalized power spectrum from the 1550 nm laser. Its magnitude is one order smaller than that in (b), implying that most of the system noise comes from the waveguide coupling, not from the laser or the power meter.

The overall NEP is calculated by measuring the device responsivity and noise spectrum density. In our characterization, the SNR is examined in frequency domain. Fourier transform is applied to the temporal waveform when there is no radiation (blue curve in Fig. 6(b)). To do a fair comparison, we quantify the relative variation, so the frequency components are scaled to its dc component for normalization, shown in Fig. 7(a). The noise modulation index is averaged at 4 Hz within 1 Hz bandwidth, which yields 9.5×10^{-5}. The corresponding NEP is calculated to be 2.59 μW/$\sqrt{}$Hz by the following equation:

$$NEP = \frac{9.5\times10^{-5}}{R_d} \cdot A_{D,} \tag{2}$$

where R_d is the device responsivity and equals 0.003945 $\mu m^2/\mu W$, A_D is the device area and equals 12.54×8.58 μm^2. The discrepancy between the calculated intrinsic NEP caused by device noise and the measured total NEP arises from the system noise that does not belong to the device itself. The system noise can come from the laser relative intensity noise, detector noise, and the mechanical instability of the experimental setup. It is found that the noise originating from the vibration of the coupling fibers is the most detrimental. Figure 7(a), 7(b), and 7(c) compare the normalized power spectrum of the light from a waveguide integrated with nanowires but not exposed to radiation (a), from a waveguide without nanowires nor exposed to radiation (b), and from the 1550 nm laser source directly (c). Compared with Fig. 7(b), the spectrum amplitude in Fig. 7(c) is one order of magnitude smaller, indicating that the laser and the optical power meter are not the main noise sources. Most of the noise is brought into the system during the fiber to the waveguide coupling, which arises from the vibration of the coupling fibers that extrude over the fiber mounts. Comparing Fig. 7(a) and 7(b), the magnitudes of power spectrum of the waveguides with and without nanowires are close to each other, meaning that the noise contributed from the nanowires is negligible and overwhelmed by the noise from the instability of waveguide coupling. Therefore, it is the mechanical instability in the fiber to the waveguide coupling that dominates the system noise and the overall noise performance. There are several ways to reduce the noise on the system side. Shortening the length of the coupling fiber extension can substantially suppress the mechanical instability. Isolating the fan vibration of the laminar flow chamber from the optical table would greatly help improve the mechanical stability. A vacuum environment can also help minimize the air flow disturbance.

Optics EXPRESS

6. Summary

In summary, we have demonstrated an uncooled plasmo-thermomechanical radiation detector that integrates suspended periodic fishbone nanowires with a waveguide. Coupling of the photonic absorption and mechanical actuation has been realized by free-standing bimetallic fishbone nanowires with unique spectral selectivity. By exploiting the interaction between the nanowires and the waveguide evanescent fields, efficient on-chip transduction of mechanical displacement to optical attenuation has been achieved, eliminating the need for the cumbersome and complex off-chip optical readouts. Although the prototype device is demonstrated at visible wavelength, the proposed design is scalable to mid-infrared or far-infrared wavelengths by modifying the dimension of the strip antennas and periods of the unit cells [30]. The bandwidth of the detector can be optimized by reducing the device thermal constant and the nanowire length. Further improvements on the characterization system can greatly reduce the system noise, so the total NEP can approach the intrinsic NEP induced by the device itself. We believe that our work which combines the advantage of the plasmonics and nanomechanics in a unique way will help push forward towards the full realization of uncooled on-chip infrared radiation detection in a high-performance, miniaturized, and power efficient way.

Appendix

Theoretical analysis of the device noise

The device noise has three main components, being the thermal fluctuation noise, background fluctuation noise, and thermal mechanical noise. Here we show the details of how to estimate the three noise components.

The thermal fluctuation noise accounts for the random fluctuation in temperature due to the statistical nature of heat exchange between the nanowires and the environment [33].

$$\overline{P_{th}} = \sqrt{4k_B T_0^2 G}, \tag{3}$$

where k_B is the Boltzmann constant 1.38×10^{-23} $m^2 \cdot kg \cdot s^{-2} \cdot K^{-1}$. The ambient temperature T_0 is assumed to be 300 K. G is the total thermal conductance from the suspended nanowire to the environment: $G = 13G_{wire} + G_{bottom} + G_{top}$ stands for the conductance through the beam, $G_{wire} = 4w\left(k_{Au}t_{Au} + k_{Ni}t_{Ni}\right)/l$. Here w = 100 nm is the nanowire width, l = 12.54 μm is the wire length, k_{Au} = 170 W/(m·K) and k_{Ni} = 60 W/(m·K) are the thermal conductivity of the gold and nickel film, and t_{Au} and t_{Ni} are the film-thickness of gold and nickel, respectively. The single wire thermal conductance is multiplied by 13 because there are 13 wires in the device. G_{bottom} accounts for the heat convection through the air gap to the substrate. Though air and SiO_2 are good thermal isolators, they still conduct a significant amount of heat due to the thin film-thickness. Assuming that the bottom Si substrate acts as a heat sink, the heat transfer coefficient h_{bottom} is estimated to be 5.6×10^4 W/(m^2·K) from the following equation:

$$\frac{1}{h_{bottom}} = \frac{1}{h_{air}} + \frac{1}{h_{SiO2}}, \tag{4}$$

where $h_{air} = k_{air} / t_{air}$, k_{air} is the air thermal conductivity and is 0.024 W/(m·K), t_{air} is the air gap and is 360 nm. $h_{SiO2} = k_{SiO2}/t_{SiO2}$, k_{SiO2} is the SiO_2 thermal conductivity and is 1.4 W/(m·K), t_{SiO2} is the SiO_2 film thickness and is 4 μm. Then $G_{bottom} = A_D \cdot FF \cdot h_{bottom}$. A_D is the device area and it is measured to be 12.54×8.58 μm^2. Since the wires are periodically spaced and only the wire area will exchange heat, the filling factor FF (0.2 in our design) is required to rule out the spacing. The same ideal can be applied to the wire top surface thermal conductance,

Optics EXPRESS

$G_{top} = A_D \cdot FF \cdot h_{top}$, here the top environment is semi-infinite air, so h_{top} = 10 W/(m^2·K). The total thermal conductance $G = 3.8 \times 10^{-6}$ W/K, and $\overline{P_{th}}$ = 4.345 pW/√Hz.

The background fluctuation noise originates from the radiative heat exchange with the environment. It is regulated by the following equation:

$$\overline{P_{rad}} = \sqrt{16 A_D \cdot FF \cdot \varepsilon \sigma k_B T^5}, \tag{5}$$

where ε is the permittivity of surroundings (assumed to be 1 for air), $\sigma = 5.67 \times 10^{-8}$ W·m^{-2}·K^{-4} is the Stefan-Boltzmann constant, and T = 300 K. Thus, $\overline{P_{rad}}$ is found to be 25.57 fW/√Hz. Compared to the thermal fluctuation noise, the background fluctuation noise is two orders of magnitude smaller, which also matches our conclusion that the radiation heat transfer is negligible in the previous part.

The thermo-mechanical noise comes from the random vibration of the nanowires. The vibration noise in y direction arising from the thermal energy can be calculated as [34]:

$$\overline{y_{vib}} = \sqrt{\frac{4k_B T}{mQ} \frac{\omega_0}{\left(\omega^2 - \omega_0^2\right)^2 + \left(\omega\omega_0 / Q\right)^2}}, \tag{6}$$

where ω_0 is the resonant frequency, m is the effective mass, and Q is the quality factor. Q = 3.054×10^6 and $\omega_0 = 8.169 \times 10^5$ Hz are extracted from simulations (COMSOL Multiphysics). For the off-resonance vibration, where $\omega << \omega_0$, the vibration noise can be simplified as:

$$\overline{y_{vib}} = \sqrt{\frac{4k_B T}{k\omega_0 Q}}, \tag{7}$$

where $k = m\omega_0^2$ is the spring constant of the nanowire. For a point-loaded double-clamped beam at the center, the spring constant is:

$$k = \frac{\pi^4}{6} \frac{Ewt^3}{l^3}. \tag{8}$$

Here, $E = (E_{Au}t_{Au} + E_{Ni}t_{Ni})/(t_{Au} + t_{Ni})$ is the equivalent Young's modulus of the nanowire, and it equals 126.8 GPa. $t = t_{Au} + t_{Ni}$ is the thickness of the nanowire. l is the length and w is the width of the wire. k is calculated to be 0.013. Correspondingly $\overline{y_{vib}}$ is 0.7145 fm/√Hz.

Recall from Ref [30]. that η_{TI} = 2.175 K/(μW/μm^2) is the temperature-IR power density conversion ratio and η_{DT} = 0.113 nm/K is the displacement-temperature conversion ratio, the noise equivalent power induced by thermo-mechanical noise can be deduced to be 312.7 pW/√Hz from the following equation:

$$\overline{P_{vib}} = \frac{\overline{y_{vib}}}{\eta_{DT}\eta_{TI}} A_D. \tag{9}$$

It is worth noting that the NEP from the device is a lower boundary estimation, because the Q factor of the nanowire should be much smaller due to thin-film gas damping and surface imperfections, whereas only the thermoelastic damping is considered in our simulations. Thermomechanical noise is dominant among all the device noise sources and can be reduced by shortening the wire length.

Optics EXPRESS

Funding

National Science Foundation (NSF) (Award No. ECCS-1449397); Defense Threat Reduction Agency (DTRA) Grant HDTRA1-16-1-0025.

References

1. A. Rogalski, "Infrared detectors: status and trends," Prog. Quantum Electron. **27**(2-3), 59–210 (2003).
2. M. A. Kinch, "Fundamental physics of infrared detector materials," J. Electron. Mater. **29**(6), 809–817 (2000).
3. P. Norton, "HgCdTe infrared detectors," Opto-Electron. Rev. **3**, 159–174 (2002).
4. A. Barve, S. Lee, S. Noh, and S. Krishna, "Review of current progress in quantum dot infrared photodetectors," Laser Photonics Rev. **4**(6), 738–750 (2010).
5. M. S. Jayalakshmy and J. Philip, "Enhancement in pyroelectric detection sensitivity for flexible $LiNbO_3$ PVDF nanocomposite films by inclusion content control," J. Polym. Res. **22**(3), 42 (2015).
6. G. Sebald, D. Guyomar, and A. Agbossou, "On thermoelectric and pyroelectric energy harvesting," Smart Mater. Struct. **18**(12), 125006 (2009).
7. A. Navid, C. S. Lynch, and L. Pilon, "Purified and porous poly(vinylidene fluoride-trifluoroethylene) thin films for pyroelectric infrared sensing and energy harvesting," Smart Mater. Struct. **19**(5), 055006 (2010).
8. Y. Pan, G. Tagliabue, H. Eghlidi, C. Höller, S. Dröscher, G. Hong, and D. Poulikakos, "A Rapid Response Thin-Film Plasmonic-Thermoelectric Light Detector," Sci. Rep. **6**(1), 37564 (2016).
9. W. Zhu, Y. Deng, and L. Cao, "Light-concentrated solar generator and sensor based on flexible thin-film thermoelectric device," Nano Energy **34**, 463–471 (2017).
10. J. P. Carmo, L. M. Goncalves, and J. H. Correia, "Thermoelectric Microconverter for Energy Harvesting Systems," IEEE Trans. Ind. Electron. **57**(3), 861–867 (2010).
11. F. O. Briano, M. Colangelo, C. Errando-Herranz, H. Sohlström, and K. B. Gylfason, "A fast uncooled infrared nanobolometer featuring a hybrid-plasmonic cavity for enhanced optical responsivity," in *2017 IEEE 30th International Conference on Micro Electro Mechanical Systems (MEMS)* (2017), pp. 932–935.
12. W. Dai, Q. Yang, F. Gu, and L. Tong, "ZnO subwavelength wires for fast-response mid-infrared detection," Opt. Express **17**(24), 21808–21812 (2009).
13. J. B. Herzog, M. W. Knight, and D. Natelson, "Thermoplasmonics: Quantifying Plasmonic Heating in Single Nanowires," Nano Lett. **14**(2), 499–503 (2014).
14. Z. Qian, S. Kang, V. Rajaram, C. Cassella, N. E. McGruer, and M. Rinaldi, "Zero-power infrared digitizers based on plasmonically enhanced micromechanical photoswitches," Nat. Nanotechnol. **12**(10), 969–973 (2017).
15. Y. Hui, J. S. Gomez-Diaz, Z. Qian, A. Alù, and M. Rinaldi, "Plasmonic piezoelectric nanomechanical resonator for spectrally selective infrared sensing," Nat. Commun. **7**, 11249 (2016).
16. M. R. Watts, M. J. Shaw, and G. N. Nielson, "Microphotonic thermal imaging," Nat. Photonics **1**(11), 632–634 (2007).
17. T. W. Kenny, W. J. Kaiser, S. B. Waltman, and J. K. Reynolds, "Novel infrared detector based on a tunneling displacement transducer," Appl. Phys. Lett. **59**(15), 1820–1822 (1991).
18. F. Zhang, Q. Shen, X. Shi, S. Li, W. Wang, Z. Luo, G. He, P. Zhang, P. Tao, C. Song, W. Zhang, D. Zhang, T. Deng, and W. Shang, "Infrared Detection Based on Localized Modification of Morpho Butterfly Wings," Adv. Mater. **27**(6), 1077–1082 (2015).
19. N. J. Hogan, A. S. Urban, C. Ayala-Orozco, A. Pimpinelli, P. Nordlander, and N. J. Halas, "Nanoparticles Heat through Light Localization," Nano Lett. **14**(8), 4640–4645 (2014).
20. H. Zhu, F. Yi, and E. Cubukcu, "Plasmonic metamaterial absorber for broadband manipulation of mechanical resonances," Nat. Photonics **10**(11), 709–714 (2016).
21. J. R. Barnes, R. J. Stephenson, C. N. Woodburn, S. J. O'Shea, M. E. Welland, T. Rayment, J. K. Gimzewski, and C. Gerber, "A femtojoule calorimeter using micromechanical sensors," Rev. Sci. Instrum. **65**(12), 3793–3798 (1994).
22. J. Lai, T. Perazzo, Z. Shi, and A. Majumdar, "Optimization and performance of high-resolution micro-optomechanical thermal sensors," Sens. Actuators Phys. **58**(2), 113–119 (1997).
23. F. Yi, H. Zhu, J. C. Reed, and E. Cubukcu, "Plasmonically Enhanced Thermomechanical Detection of Infrared Radiation," Nano Lett. **13**(4), 1638–1643 (2013).
24. J. Agustí Batlle and G. Abadal Berini, *Nonlinear Micro/Nano-Optomechanical Oscillators for Energy Transduction from IR Sources* (Universitat Autònoma de Barcelona, 2015).
25. L. Ding, C. Baker, P. Senellart, A. Lemaitre, S. Ducci, G. Leo, and I. Favero, "High Frequency GaAs Nano-Optomechanical Disk Resonator," Phys. Rev. Lett. **105**(26), 263903 (2010).
26. E. Gavartin, P. Verlot, and T. J. Kippenberg, "A hybrid on-chip optomechanical transducer for ultrasensitive force measurements," Nat. Nanotechnol. **7**(8), 509–514 (2012).
27. Y.-W. Hu, Y.-F. Xiao, Y.-C. Liu, and Q. Gong, "Optomechanical sensing with on-chip microcavities," Front. Phys. **8**(5), 475–490 (2013).
28. Q. Zhao, C. Guclu, Y. Huang, F. Capolino, and O. Boyraz, "Experimental Demonstration of Directive Si3N4 Optical Leaky Wave Antennas With Semiconductor Perturbations," J. Lightwave Technol. **34**(21), 4864–4871 (2016).

Optics EXPRESS

29. L. Chen, C. R. Doerr, L. Buhl, Y. Baeyens, and R. A. Aroca, "Monolithically Integrated 40-Wavelength Demultiplexer and Photodetector Array on Silicon," IEEE Photonics Technol. Lett. **23**(13), 869–871 (2011).
30. Q. Zhao, P. Sadri-Moshkenani, M. W. Khan, R. Torun, and O. Boyraz, "On-Chip Bimetallic Plasmo-Thermomechanical Detectors for Mid-Infrared Radiation," IEEE Photonics Technol. Lett. **29**(17), 1459–1462 (2017).
31. Q. Zhao, M. W. Khan, P. Sadri-Moshkenani, R. Regan, F. Capolino, and O. Boyraz, "Demonstration of a Plasmo-Thermomechanical Radiation Detector with Si3N4 Waveguide Optical Readout Circuit," in *Conference on Lasers and Electro-Optics (2018), Paper JW2A.175* (Optical Society of America, 2018), p. JW2A.175.
32. P. Eriksson, J. Y. Andersson, and G. Stemme, "Thermal characterization of surface-micromachined silicon nitride membranes for thermal infrared detectors," J. Microelectromech. Syst. **6**(1), 55–61 (1997).
33. "Uncooled Thermal Imaging Arrays, Systems, and Applications | (2001) | Kruse | Publications | Spie," https://spie.org/publications/book/415351?SSO=1.
34. E. Majorana and Y. Ogawa, "Mechanical thermal noise in coupled oscillators," Phys. Lett. A **233**(3), 162–168 (1997).